Rare Met. (2022) 41(7):2259–2267
https://doi.org/10.1007/s12598-021-01934-7

RARE METALS

ORIGINAL ARTICLE

Rational design of $Sn_4P_3/Ti_3C_2T_x$ composite anode with enhanced performance for potassium-ion battery

Jie Zhao, Chao-Lin Li*, Gang Chen, Fei Ji, Yi-Yong Shen, Juan Peng, Wen-Hui Wang*

Received: 9 August 2021 / Revised: 23 October 2021 / Accepted: 27 October 2021 / Published online: 3 March 2022

Abstract The potential application of high-capacity Sn_4P_3 anode for potassium-ion batteries (PIBs) is hindered by the poor cycle stability mainly rooted from the huge volume changes upon cycling and low electronic conductivity. To address the above issues, sandwich-like structured $Sn_4P_3/Ti_3C_2T_x$ was designed and synthesized as anode material for PIBs. As a result, $Sn_4P_3/Ti_3C_2T_x$ presents superior cycle stability (retains a capacity of 103.2 $mAh·g^{-1}$ even after 300 cycles at 1000 $mA·g^{-1}$) and rate capability (delivers 60.7 $mAh·g^{-1}$ at high current density of 2000 $mA·g^{-1}$). The excellent electrochemical performance of sandwich-like structured $Sn_4P_3/Ti_3C_2T_x$ is originated from the synergistic effect between Sn_4P_3 and $Ti_3C_2T_x$, where $Ti_3C_2T_x$ acts as a conductive matrix to facilitate electron transfer and buffer the volume change of Sn_4P_3 particles upon cycling, while Sn_4P_3 serves as pillars to prevent the collapse and stacking of $Ti_3C_2T_x$ sheets. Moreover, significant capacitive contribution is demonstrated as a major contributor to the excellent rate capability.

Keywords Sn_4P_3; $Ti_3C_2T_x$; Anode material; Potassium-ion battery

1 Introduction

With the spread of portable electronic devices and the boom in the new energy vehicle industry, there is an urgent need to develop energy storage devices with high performance and low cost [1, 2]. Due to the high energy density and good cycle stability, lithium-ion batteries (LIBs) have accounted for most of the consumer battery market. However, the limited resources of lithium ore and its uneven global distribution limit its use in large-scale energy storage applications [3]. Considering the high natural abundance of potassium (2.09 wt%, while 0.0017 wt% for Li) and the similar energy storage mechanism to that of LIBs, potassium-ion batteries (PIBs) have attracted much attention as a promising alternative to LIBs [4–6]. However, the larger K^+ radius (0.138 nm) leads to slow reaction kinetics and larger volume changes of active material during cycling [7]. Up to now, the development of PIBs is still in its infancy and electrode materials with high capacity and good cycling stability are yet to be developed [8, 9].

Graphite is the most extensively used anode material with excellent electrical conductivity, and large layer spacing (3.4 nm) [10]. Unfortunately, the practical application of graphite anode material remains challenging mainly due to its low capacity. In this regards, alloy-based materials are potential alternatives due to their high capacity. Among the alloy-based materials, Sn_4P_3, which

Supplementary Information The online version contains supplementary material available at https://doi.org/10.1007/s12598-021-01934-7.

J. Zhao, C.-L. Li*, W.-H. Wang*
School of Civil and Environmental Engineering, Harbin Institute of Technology, Shenzhen 518055, China
e-mail: lichaolin@hit.edu.cn

W.-H. Wang
e-mail: wangwenhui@hit.edu.cn

J. Zhao, G. Chen, F. Ji, Y.-Y. Shen, J. Peng
Shenzhen Environmental Technology Group Co. Ltd., Shenzhen 518049, China

C.-L. Li
State Key Laboratory of Urban Water Resource and Environment, School of Environment, Harbin Institute of Technology, Harbin 150090, China

possesses a high theoretical capacity of 612 mAh·g^{-1} and synergistic benefits of Sn and P, is deemed as the most promising anode for PIBs [11–13]. However, the low electronic conductivity (30.7 S·cm^{-1}) and huge volume changes during charge/discharge process lead to sluggish reaction kinetics and poor cycling stability [12, 14–16]. To tackle these limitations, an effective strategy is to combine Sn_4P_3 with highly conductive skeleton [16–18]. For instance, Zhang et al. [12] prepared Sn_4P_3/C composite via ball-milling technique and studied it as anode for PIBs, which delivers a reversible capacity of 384.8 mAh·g^{-1} at 50 mA·g^{-1}. However, the Sn_4P_3-based composites prepared by the ball-milling method are poor in terms of cycle stability [14, 19, 20]. The capacity retention of Sn_4P_3/C composite is only ~ 6.6% after 120 cycles. Therefore, further efforts are still needed to achieve high capacity, long-term cycle stability as well as high-rate performance.

$Ti_3C_2T_x$, as a new member of two-dimensional layered material family, has shown unique advantages in the field of energy storage due to its layered structure, superior electrical conductivity (6500 S·cm^{-1}), and low diffusion barrier [21–25]. Intensive study has been performed on the use of $Ti_3C_2T_x$ as electrode materials for energy storage batteries, such as hybrid Ti_3C_2/NiCoP for sodium ion batteries [26], Ti_3C_2/Si composite for LIBs [27], and MoS_2/MXene hybrids for PIBs [28]. Yet, incorporating MXene with high capacity Sn_4P_3 anode has rarely been tried.

Herein, we prepared a novel sandwich-like structured $Sn_4P_3/Ti_3C_2T_x$ composite, which has rarely been reported before, via a solvothermal reaction followed by phosphorization process. Electrochemical study demonstrates that $Sn_4P_3/Ti_3C_2T_x$ owns superior cycle stability and rate capability, which benefits from the synergistic effect between Sn_4P_3 and $Ti_3C_2T_x$. In $Sn_4P_3/Ti_3C_2T_x$ composite, $Ti_3C_2T_x$ acts as a conductive matrix to facilitate electron transfer and buffer the volume change of Sn_4P_3 particles during charge/discharge, while Sn_4P_3 serves as pillars to prevent the collapse and stacking of $Ti_3C_2T_x$ sheets.

2 Experimental

Except for $Ti_3C_2T_x$ powder was purchased from Jilin 11 Technology Co., Ltd, all other materials used in this experiment were purchased from Shanghai Macklin Biochemical Co., Ltd.

2.1 Synthesis of $Sn_4P_3/Ti_3C_2T_x$

In a typical preparation, $SnCl_2·2H_2O$ and $Ti_3C_2T_x$ powder with different mass ratios of 1:0.5, 1:1 and 1:2 were added into ethanol solution, followed by an ultrasonic treatment process for 1 h. Afterward, 20 ml NaOH solution with concentration of 0.2 mol·L^{-1} was added into the above mixture and stirred for 0.5 h. The solution was subsequently transferred into Teflon-lined stainless-steel autoclave and reacted at 180 °C for 10 h. The obtained SnO/$Ti_3C_2T_x$ powder was then washed with deionized water and collected by freeze-drying. To get $Sn_4P_3/Ti_3C_2T_x$, appropriate $NaH_2PO_2·H_2O$ and SnO/$Ti_3C_2T_x$ powder were

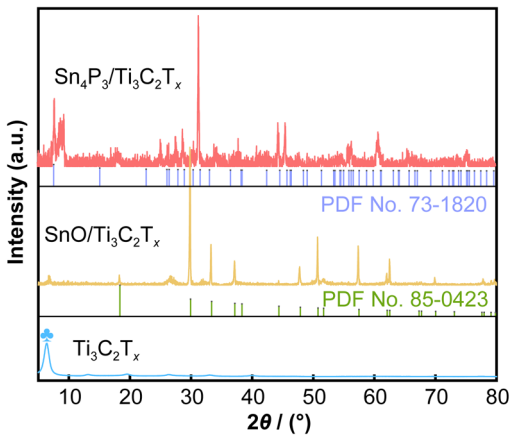

Fig. 2 XRD patterns of $Ti_3C_2T_x$, SnO/$Ti_3C_2T_x$, and $Sn_4P_3/Ti_3C_2T_x$

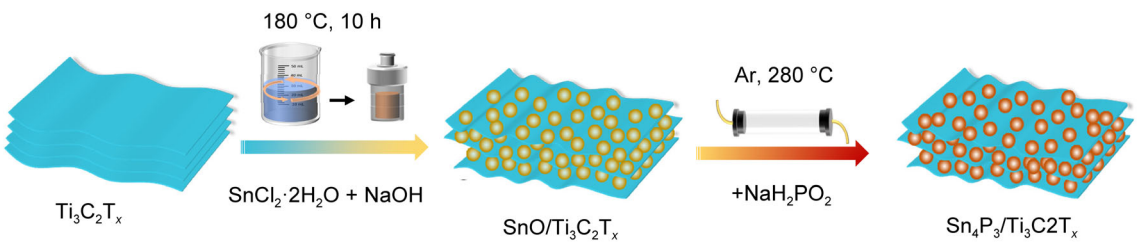

Fig. 1 Schematic illustration of synthesis process of $Sn_4P_3/Ti_3C_2T_x$ composite

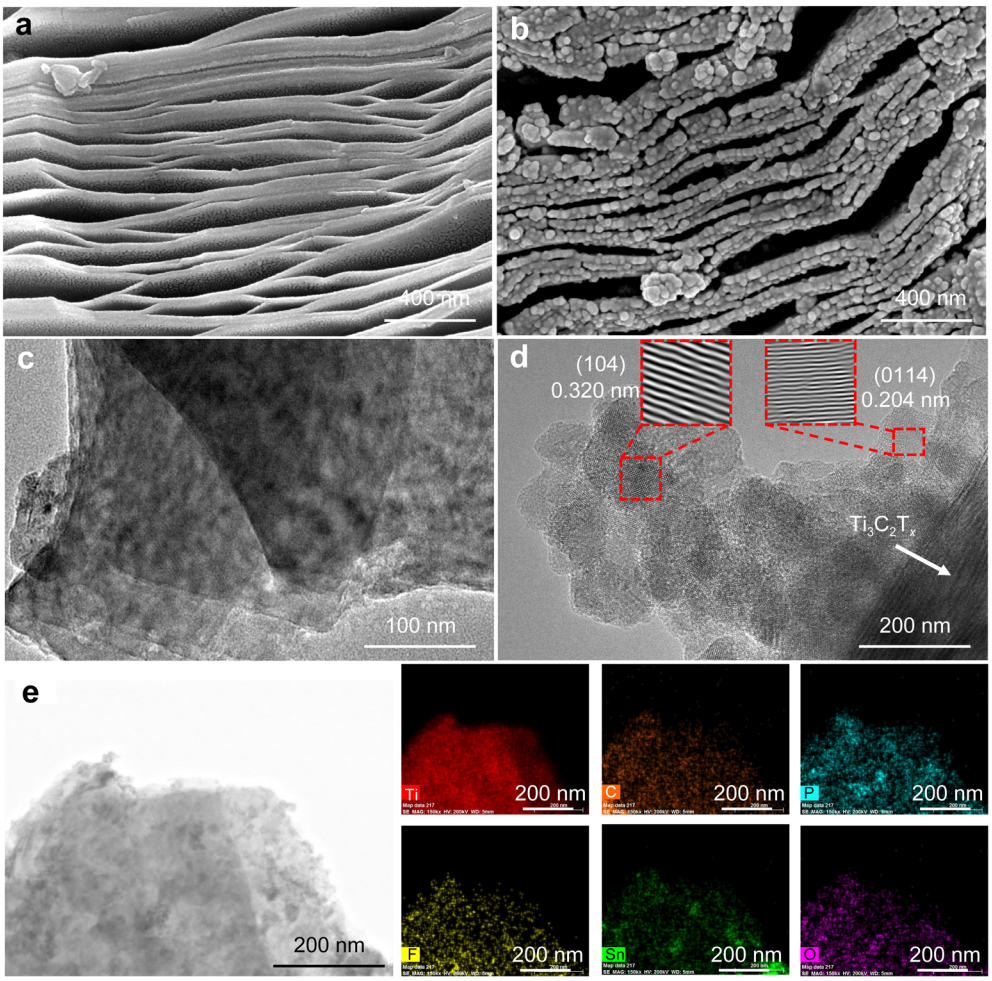

Fig. 3 SEM images of **a** $Ti_3C_2T_x$ and **b** $Sn_4P_3/Ti_3C_2T_x$; **c** TEM image of $Ti_3C_2T_x$; **d** HRTEM images and (inset) FFT pattern of $Sn_4P_3/Ti_3C_2T_x$; **e** TEM image and corresponding elemental mappings of $Sn_4P_3/Ti_3C_2T_x$

annealed in tube furnace in Ar atmosphere with temperature of 280 °C for 0.5 h. Electrochemical results in Fig. S1 show that the $Sn_4P_3/Ti_3C_2T_x$ sample with an initial $SnCl_2{\cdot}2H_2O$ to $Ti_3C_2T_x$ mass ratio of 1:1 possesses the optimal performance. Therefore, it was selected for further research. As a control, bare Sn_4P_3 was prepared in the same process without adding $Ti_3C_2T_x$ powder.

2.2 Material characterizations

The crystal structure, composition and morphology of the samples were investigated by X-ray diffraction (XRD, Rigaku, Ultima IV) with Cu Kα radiation, X-ray photoelectron spectroscopy (XPS, Thermo Scientific K-Alpha), scanning electron microscope (SEM, Zeiss Sigma 300), and transmission electron microscope (TEM, JEOL JEM 2100F), respectively.

2.3 Electrochemical characterizations

The electrode was fabricated by coating the mixed slurry of 80 wt% of the as-prepared $Sn_4P_3/Ti_3C_2T_x$ or bare Sn_4P_3, 10 wt% carbon black, and 10 wt% polyvinylidene fluoride (PVDF) binder in N-methyl pyrrolidone (NMP) onto the copper foil. The electrodes were then vacuum-dried at 85 °C for 12 h and cut into disks with loading of ~ 0.8 $mg{\cdot}cm^{-2}$. Electrochemical performance was measured with CR2032-type coin cells, where K foil works as counter/reference electrode and KPF_6 in ethylene carbonate/diethyl carbonate works as electrolyte. Galvanostatic charge–discharge (GCD) was tested on a Land CT2001A battery testing system. Cyclic voltammograms (CV) and electrochemical impedance spectroscopy (EIS) tests were carried out at CHI660e electrochemistry workstation. CV was conducted in a voltage range of 0.01–2.00 V. EIS was tested over a frequency range from

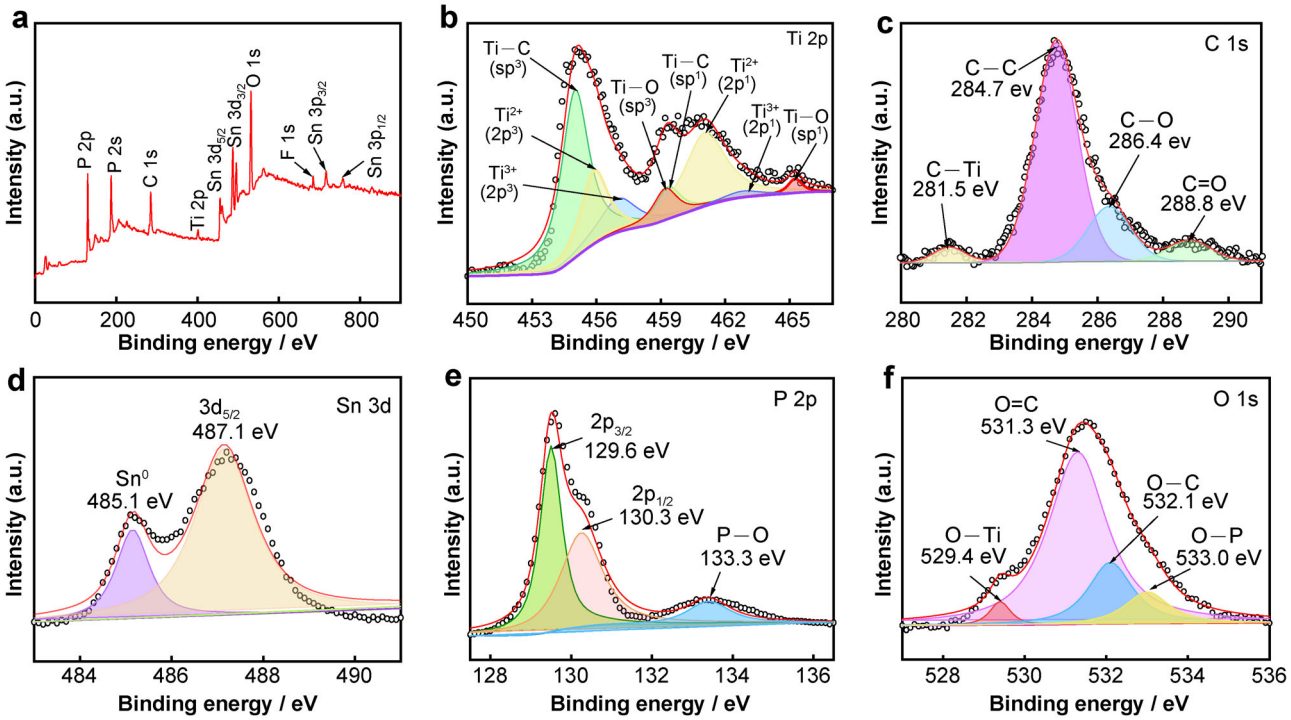

Fig. 4 XPS spectra of $Sn_4P_3/Ti_3C_2T_x$: **a** full-scan survey, **b** Ti 2p, **c** C 1s, **d** Sn 3d, **e** P 2p and **f** O 1s

10 mHz to 100 kHz by applying an alternating current (AC) signal of 5 mV.

3 Results and discussion

Figure 1 illustrates the synthesis process of $Sn_4P_3/Ti_3C_2T_x$ composite. Firstly, SnO nanoparticles are loaded on the surface of $Ti_3C_2T_x$ by a hydrothermal reaction. Afterward, in situ phosphorization reaction is conducted in a tube furnace and the $Sn_4P_3/Ti_3C_2T_x$ composite material is finally obtained.

The crystal structures of the materials were investigated by XRD. As shown in Fig. 2, the defined peaks at ~ 6.46° could be assigned to (002) planes of titanium carbide, which agrees well with previous reports [29–31]. In the XRD pattern of final product of $Sn_4P_3/Ti_3C_2T_x$, the diffraction peaks locating at ~ 27.7°, 28.8°, 30.3, 31.4°, 44.5°, 45.7° and 56.5° are indexed as (104), (015), (0012), (107), (0114), (110) and (027) planes of rhombohedral Sn_4P_3 (JCPDS No. 73-1820) respectively [15, 32], while the extra peaks can be attributed to $Ti_3C_2T_x$, indicating the successful coupling of Sn_4P_3 and $Ti_3C_2T_x$.

Morphology of pristine $Ti_3C_2T_x$ and the product of $Sn_4P_3/Ti_3C_2T_x$ was investigated by SEM. Figure 3a shows the SEM image of $Ti_3C_2T_x$, in which a typical accordion-like and well-aligned layered structure is clearly observed. The layered structure still maintains even after a long time of hydrothermal reaction and high-temperature phosphating process (Fig. 3b), suggesting the excellent structural stability of $Ti_3C_2T_x$. Moreover, Sn_4P_3 nanoparticles are evenly distributed on the surface of $Ti_3C_2T_x$ sheets, thus forming a sandwich-like structure (Fig. S2). In this structure, Sn_4P_3 nanoparticles can act as pillars to prevent the collapse and stacking of $Ti_3C_2T_x$ sheets, while the $Ti_3C_2T_x$ sheets could provide a good conductive matrix and unblocked channels for electron transmission and K^+ transfer, respectively, thereby achieving synergistic effect. TEM images were collected to reveal the structural and morphological details of $Ti_3C_2T_x$ and $Sn_4P_3/Ti_3C_2T_x$ composite. As shown in Fig. 3c, obvious multilayer structure is observed for matrix. Figure 3d shows high-resolution transmission electron microscope (HRTEM) image and fast Fourier transformation (FFT) pattern of $Sn_4P_3/Ti_3C_2T_x$, clear fringes with lattice spacing of 0.320 and 0.204 nm are observed, corresponding to (104) and (0114) planes of Sn_4P_3, respectively. HRTEM images in Fig. S3 reveal the expansion of the interlayer spacing from $Ti_3C_2T_x$ to $Sn_4P_3/Ti_3C_2T_x$, which is mainly caused by the insertion of cations between the layers during synthesis process. Elemental mappings in Fig. 3e suggest

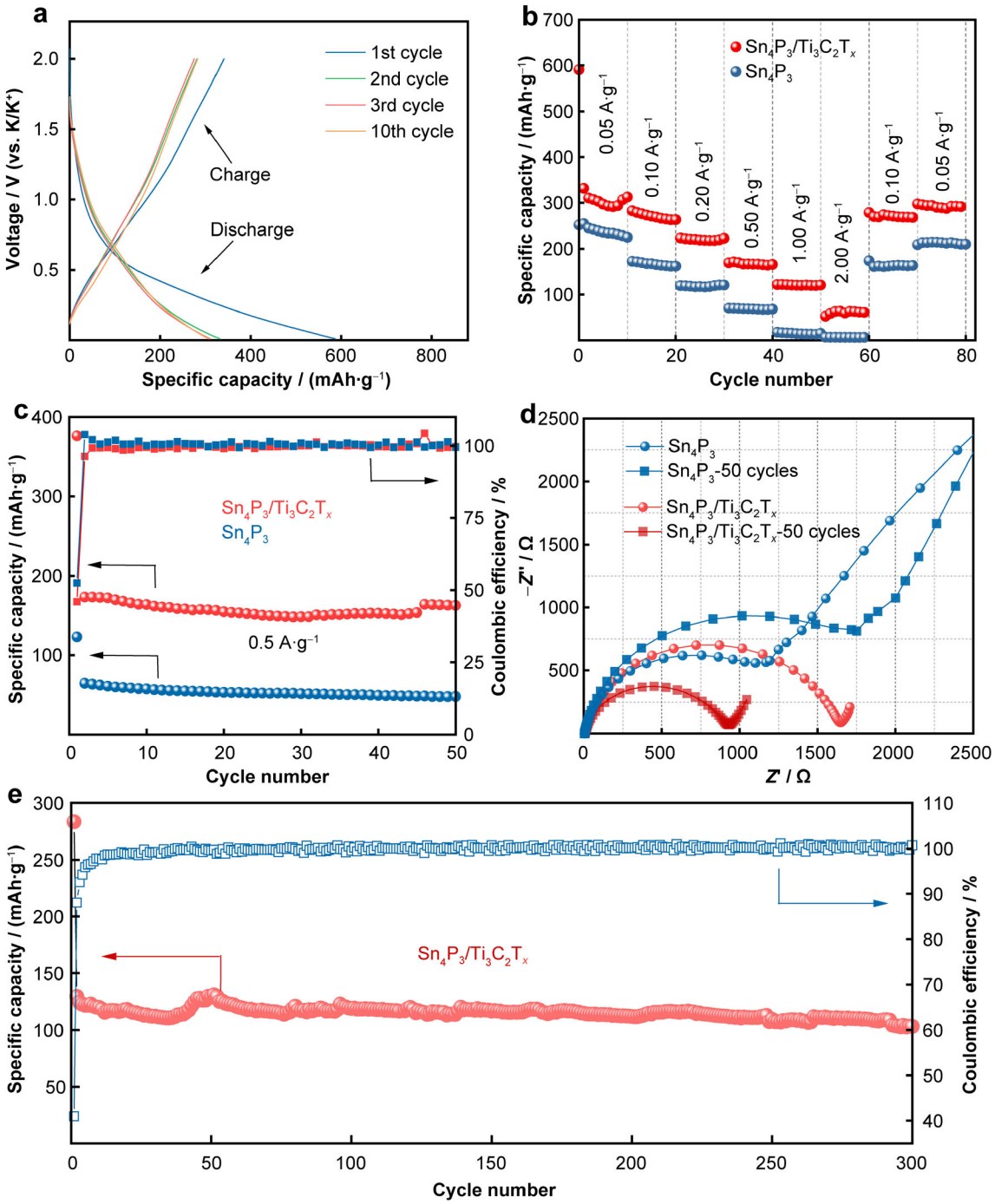

Fig. 5 **a** Selected galvanostatic charge/discharge profiles of $Sn_4P_3/Ti_3C_2T_x$ at current density of 50 $mA{\cdot}g^{-1}$; **b** rate capability and **c** cycle performance of Sn_4P_3 and $Sn_4P_3/Ti_3C_2T_x$ electrodes at 500 $mA{\cdot}g^{-1}$; **d** Nyquist plots of Sn_4P_3 and $Sn_4P_3/Ti_3C_2T_x$ electrodes before and after 50 cycles; **e** long-term cycling performance of $Sn_4P_3/Ti_3C_2T_x$ electrode at 1 $A{\cdot}g^{-1}$ (working voltage of 0.01–2.00 V)

that Sn_4P_3 particles are homogeneously distributed on the matrix of $Ti_3C_2T_x$.

The chemical states of different elements in $Sn_4P_3/Ti_3C_2T_x$ composite were analyzed by XPS. Figure 4a shows the full-scan spectrum of $Sn_4P_3/Ti_3C_2T_x$ sample, demonstrating the existence of Ti, C, Sn, P, O and F. Figure 4b–f exhibits the high-resolution XPS spectra of Ti 2p, C 1s, Sn 3d, P 2p and O 1s, respectively. Ti 2p spectrum in Fig. 4b can be deconvoluted into four species of Ti^{2+}, Ti^{3+}, Ti–C and Ti–O, which is consistent with the previous literatures [33, 34]. Figure 4c displays four peaks at ~ 281.5, 284.7, 286.4 and 288.8 eV, which are assigned to the characteristic bonds of C–Ti, C–C, C–O and C=O, respectively. In terms of Sn 3d spectrum in Fig. 4d, the

peak at ~ 487.1 eV is resulted from spin-orbital splitting photoelectrons of Sn, which is relevant to the Sn–P bond of Sn_4P_3 phase. While another peak situated at ~ 485.1 eV corresponds to Sn^0 [35, 36]. As displayed in Fig. 4e, P 2p spectrum is divided into three peaks. Two peaks locating at ~ 129.6 and 130.3 eV are related to typical P $2p_{3/2}$ and P $2p_{1/3}$, corresponding to P–Sn bond of Sn_4P_3 phase. While the small peak at ~ 133.3 eV is attributed to P–O bond, indicating that the oxidized phosphate species remain on the surface of $Sn_4P_3/Ti_3C_2T_x$. For O 1s spectrum in Fig. 4f, the peaks at ~ 529.4, 531.3, 532.1 and 533.0 eV correspond to O–Ti, O=C, O–C and O–P, respectively. XPS results further illustrate that $Sn_4P_3/Ti_3C_2T_x$ composite was synthesized successfully.

To evaluate potassium storage properties, the Sn_4P_3 and $Sn_4P_3/Ti_3C_2T_x$ were investigated by using CR2032-type coin cells, in which potassium foils were used as counter/reference electrodes. CV was firstly carried out at a scan rate of 0.1 $mV{\cdot}s^{-1}$ with the potential window between 0.01 and 2.00 V. As shown in Fig. S4, a broad peak between 0.01 and 1.00 V is observed in the initial cathodic scan, which is derived from the potassiation reaction to form K-P and K-Sn phases as well as the formation of solid electrolyte interphase (SEI). In the following anodic scan, a weak peak centered at 0.8 V can be observed, corresponding to the de-potassiation process. The second and third CV curves overlap with each other, indicating the good reversibility of $Sn_4P_3/Ti_3C_2T_x$ during charge and discharge.

Figure 5a shows the selected charge/discharge profiles at current density of 50 $mA{\cdot}g^{-1}$ between 0.01 and 2.00 V (vs. K/K^+). In the first cycle, $Sn_4P_3/Ti_3C_2T_x$ electrode delivers a discharge and charge capacity of 586.6 and 340.9 $mAh{\cdot}g^{-1}$, respectively, corresponding to an initial Coulombic efficiency of ~ 58%. The irreversible loss of the initial capacity is mainly resulted from the formation of SEI films on the surface of the electrode material [37]. In the subsequent cycles, $Sn_4P_3/Ti_3C_2T_x$ gives stable capacity of ~ 304.8 $mAh{\cdot}g^{-1}$ and the Coulombic efficiency reaches up to > 98%. Compared with $Sn_4P_3/Ti_3C_2T_x$ composite electrode, the capacity of Sn_4P_3 electrode is only ~ 228 $mAh{\cdot}g^{-1}$ under the same current density.

Rate capability of pure Sn_4P_3 and $Sn_4P_3/Ti_3C_2T_x$ composite was measured at various current densities ranging from 0.05 to 2.00 $A{\cdot}g^{-1}$. As shown in Fig. 5b, $Sn_4P_3/Ti_3C_2T_x$ composite delivers reversible capacities of 304.8, 270.7, 220.3, 167.4, 120.8 and 60.7 $mAh{\cdot}g^{-1}$ at current densities of 0.05, 0.10, 0.20, 0.50, 1.00 and 2.00 $A{\cdot}g^{-1}$, respectively, which is obviously superior to that of pure Sn_4P_3. In addition, most of the capacity is recovered (~ 292.5 $mAh{\cdot}g^{-1}$) when the current density returns to 0.05 $A{\cdot}g^{-1}$, demonstrating that the electrode is able to accommodate the massive current changes in application. It is worth mentioning that the rate capability of $Sn_4P_3/Ti_3C_2T_x$ presented in our work surpasses Sn-based anodes reported previously (Fig. S5) [38–40], which is mainly due to that the accordion-like skeleton with good conductivity allows easy penetration of electrolyte and transfer of electrons.

Cycling performance of the bare Sn_4P_3 and $Sn_4P_3/Ti_3C_2T_x$ was compared at 0.5 $A{\cdot}g^{-1}$ in Fig. 5c. $Sn_4P_3/Ti_3C_2T_x$ electrode delivers a charge capacity of 173.1 $mAh{\cdot}g^{-1}$ for the first cycle, which is significantly higher than 64.5 $mAh{\cdot}g^{-1}$ obtained from Sn_4P_3 electrode. Moreover, the $Sn_4P_3/Ti_3C_2T_x$ electrode retains a high capacity of 162.6 $mAh{\cdot}g^{-1}$ with capacity retention of ~ 94% after 50 cycles. By contrast, the capacity of bare Sn_4P_3 electrode decays quickly with cycling and only 48.2 $mAh{\cdot}g^{-1}$ is remained at 50th cycle. Nyquist plots were collected and exhibited in Fig. 5d. It can be clearly seen that the charge transfer resistance of $Sn_4P_3/Ti_3C_2T_x$ decreases with cycling, due to the activation of electrode [14]. Whereas the Sn_4P_3 electrode shows larger impedance after 50 cycles, which is attributed to the pulverization and exfoliation of Sn_4P_3 particles (details will be presented by ex-situ SEM shown in Fig. 6). The smaller resistance well accounts for the excellent cycling stability and rate capability of $Sn_4P_3/Ti_3C_2T_x$ composite. Long-term cycle performance of $Sn_4P_3/Ti_3C_2T_x$ was further evaluated at a current density of 1.0 $A{\cdot}g^{-1}$. As displayed in Fig. 5e, $Sn_4P_3/Ti_3C_2T_x$ electrode still delivers a specific capacity of 103.2 $mAh{\cdot}g^{-1}$ even after 300 cycles, which is ~ 81% of its initial reversible capacity.

To further explore the reason for the largely improved potassium storage performance of $Sn_4P_3/Ti_3C_2T_x$ composite, morphology of the electrodes before and after cycling was studied by SEM. As shown in Fig. 6a, c, both Sn_4P_3 and $Sn_4P_3/Ti_3C_2T_x$ electrodes present flat surface before cycling. While after 50 cycles, cracks are clearly observed in Sn_4P_3 electrode (Fig. 6b). In sharp contrast, the surface of $Sn_4P_3/Ti_3C_2T_x$ electrode remains flat and intact, except for some fibers from glass fiber separator (Fig. 6d). These results reveal that the introduction of $Ti_3C_2T_x$ could effectively alleviate the stress induced by volume change during charge/discharge, thus enabling the integrity of electrode and fast transfer of electrons, which contribute greatly to the electrochemical performance (Fig. 6e, f).

Reaction kinetics of $Sn_4P_3/Ti_3C_2T_x$ electrode was analyzed by CV. As shown in Fig. 7a, the intensity of peaks increases with the scanning rate increasing from 0.2 to 1.0 $mV{\cdot}s^{-1}$. However, the CV curves always maintain a similar shape, which means that $Sn_4P_3/Ti_3C_2T_x$ electrode owns good response ability under fast scanning rate. Diffusion and capacitive contribution are qualitatively determined by the relationship between current (i) and scan rate (v) according to the following equations:

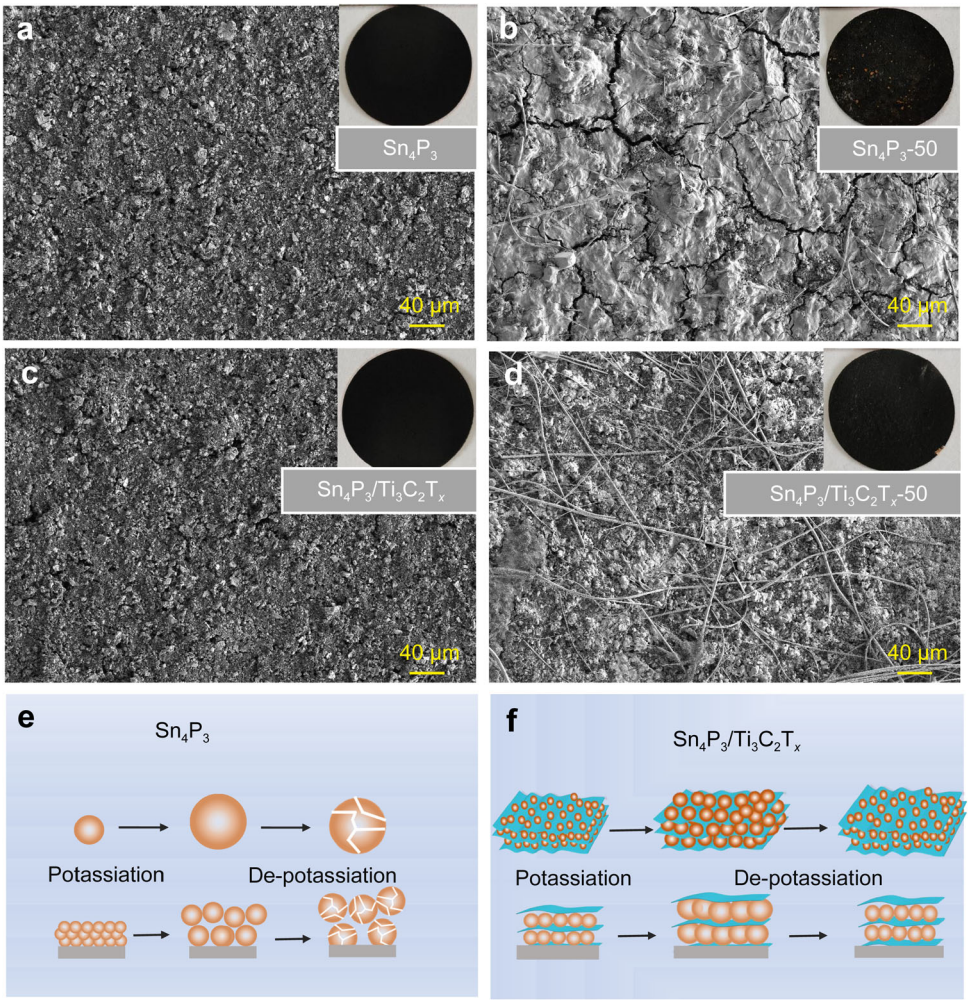

Fig. 6 SEM images of **a** initial and **b** 50 charge/discharge cycled Sn_4P_3 electrodes; **c** initial and **d** 50 charge/discharge cycled $Sn_4P_3/Ti_3C_2T_x$ electrodes (insets being digital photos of each electrode); Schematic illustration of potassiation process and de-potassiation of **e** Sn_4P_3 and **f** $Sn_4P_3/Ti_3C_2T_x$

$$i = av^b \tag{1}$$

$$\lg i = b \lg v + \lg a \tag{2}$$

where a and b are adjustable constants, and the value of b can be confirmed by the slope of lg$i$-lg$v$ curves. When the value of b is close to 0.5 or 1.0, the reaction process is diffusion control or capacitance control, respectively. As depicted in Fig. 7b, the calculated b values of the anodic and cathodic peaks are 0.86 and 0.75 respectively, which implies that the electrochemical reaction process is controlled by both diffusion and capacitance behavior. The ratios of diffusion and capacitive contribution are obtained based on the following equation:

$$i_{(V)} = k_1 v + k_2 v^{1/2} \tag{3}$$

where $k_1 v$ and $k_2 v^{1/2}$ correspond to the contributions of the capacitive effect and diffusion-controlled process, respectively. As illustrated in Figs. 7c, d and S6, the ratio of capacitive contribution gradually increases with the increase of scanning rate. This demonstrates that the electrochemical reaction process of the $Sn_4P_3/Ti_3C_2T_x$ electrode is mainly controlled by the capacitive behavior at high rate, which is beneficial for rate performance.

4 Conclusion

In summary, sandwich-like structured $Sn_4P_3/Ti_3C_2T_x$ composite was synthesized via solvothermal reaction along with low-temperature phosphating process. The electrochemical properties of $Sn_4P_3/Ti_3C_2T_x$ composite is evaluated as anode for PIBs. The introduction of the highly conductive $Ti_3C_2T_x$ matrix not only provides channels for fast electron transfer, but also alleviates the volume change of Sn_4P_3 upon charge/discharge. Moreover, the loading of Sn_4P_3 nanoparticles serves as pillars to prevent $Ti_3C_2T_x$

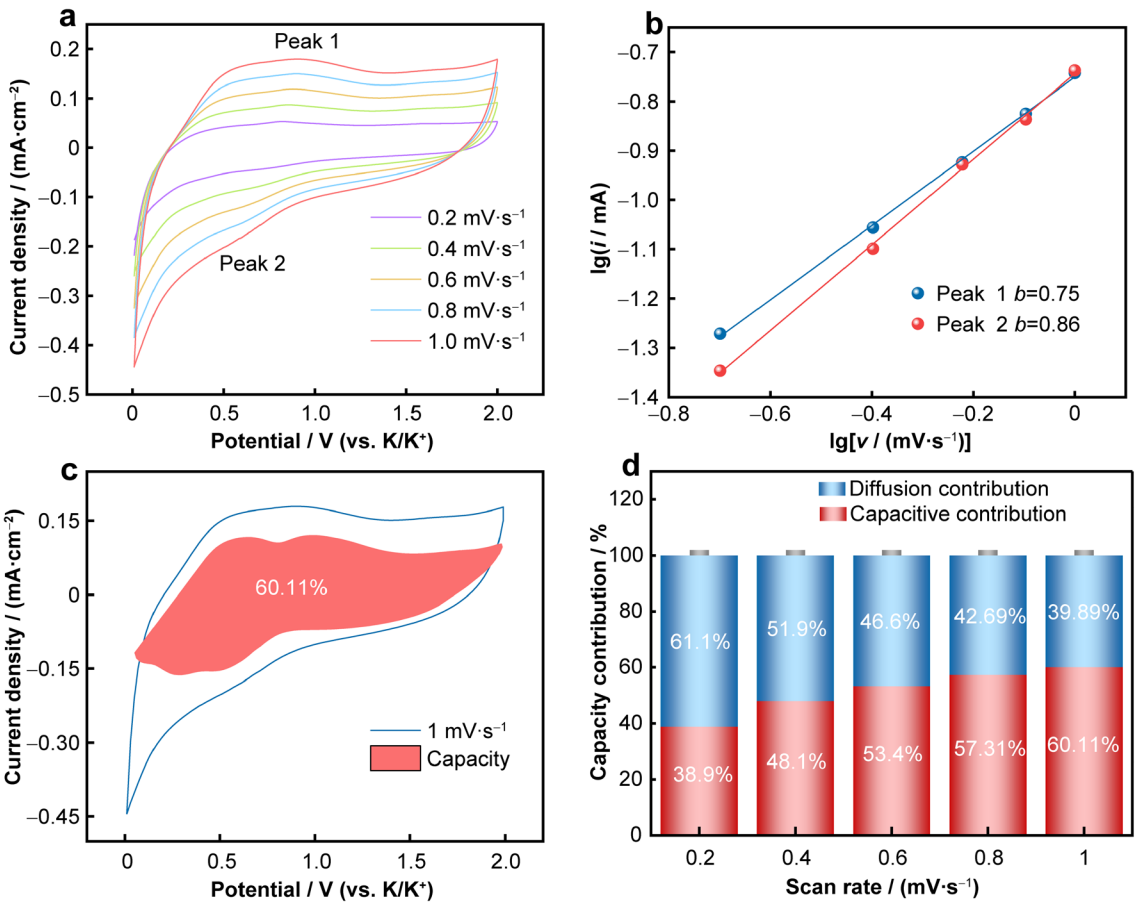

Fig. 7 **a** CV curves of $Sn_4P_3/Ti_3C_2T_x$ electrode at various scan rates; **b** lg*i*-lg*v* plots obtained from corresponding CV curves; **c** capacitive charge storage contribution at 1 mV·s^{-1}; **d** separation of contributions from capacitive- and diffusion-controlled capacities at various scan rates

sheets from collapse or stack. Owing to the synergistic effect between the two components, $Sn_4P_3/Ti_3C_2T_x$ exhibits significantly improved electrochemical performance than Sn_4P_3, which can be ranked as a high-performance anode material for PIBs.

Acknowledgments This work was financially supported by the National Natural Science Foundation of China (No. 52100084) and Shenzhen Natural Science Fund (No. GXWD20201230155427003-20200824094017001).

Declarations

Conflict of interests The authors declare that they have no conflict of interest.

References

[1] Chu S, Majumdar A. Opportunities and challenges for a sustainable energy future. Nature. 2012;488(7411):294.
[2] Dunn B, Kamath H, Tarascon JM. Electrical energy storage for the grid: a battery of choices. Science. 2011;334(6058):928.
[3] Xia MT, Chen BJ, Gu F, Zu LH, Xu MZ, Feng YT, Wang ZJ, Zhang HJ, Zhang C, Yang JH. $Ti_3C_2T_x$ MXene nanosheets as a robust and conductive tight on si anodes significantly enhance electrochemical lithium storage performance. ACS Nano. 2020;14(4):5111.
[4] Xiong PX, Wu JX, Zhou MF, Xu YH. Bismuth-antimony alloy nanoparticle@porous carbon nanosheet composite anode for high-performance potassium-ion batteries. ACS Nano. 2020;14(1):1018.
[5] Zhou JH, Guo SJ. Carbon-based anode materials for potassium-ion batteries: From material, mechanism to performance. SmartMat. 2021;2(2):176.
[6] Liang JM, Zhang LJ, Xili DG, Kang J. Research progress on tin-based anode materials for sodium ion batteries. Rare Met. 2020;39(9):1005.
[7] Zhou MF, Bai PX, Ji X, Yang JX, Wang CS, Xu YH. Electrolytes and interphases in potassium ion batteries. Adv Mater. 2021;33(7):e2003741.
[8] Li X, Qi SH, Zhang WC, Feng YZ, Ma JM. Recent progress on FeS_2 as anodes for metal-ion batteries. Rare Met. 2020;39(11):1239.
[9] Qi SH, Deng JW, Zhang WC, Feng YZ, Ma JM. Recent advances in alloy-based anode materials for potassium ion batteries. Rare Met. 2020;39(9):970.
[10] Ma JM, Li YT. Editorial for advanced energy storage and conversion materials and technologies. Rare Met. 2020;39(9):967.

[11] Zhang WC, Pang WK, Sencadas V, Guo ZP. Understanding high-energy-density Sn_4P_3 anodes for potassium-ion batteries. Joule. 2018;2(8):1534.
[12] Zhang WC, Mao JF, Li S, Chen ZX, Guo ZP. Phosphorus-based alloy materials for advanced potassium-ion battery anode. J Am Chem Soc. 2017;139(9):3316.
[13] Lei KX, Wang J, Chen C, Li SY, Wang SW, Zheng SJ, Li FJ. Recent progresses on alloy-based anodes for potassium-ion batteries. Rare Met. 2020;39(9):989.
[14] Li DP, Zhang YM, Sun Q, Zhang SN, Wang ZP, Liang Z, Si PC, Ci LJ. Hierarchically porous carbon supported Sn_4P_3 as a superior anode material for potassium-ion batteries. Energy Storage Mater. 2019;23:367.
[15] Ran LB, Gentle I, Lin TE, Luo B, Mo N, Rana M, Li M, Wang LZ, Knibbe R. Sn_4P_3@porous carbon nanofiber as a self-supported anode for sodium-ion batteries. J Power Sources. 2020; 461:228116.
[16] Wang WH, Zhang JL, Yu DYW, Li Q. Improving the cycling stability of Sn_4P_3 anode for sodium-ion battery. J Power Sources. 2017;364:420.
[17] Zhang JL, Li CL, Wang WH, Yu DYW. Facile synthesis of hollow Cu_3P for sodium-ion batteries anode. Rare Met. 2021; 40(12):3460.
[18] Qian JF, Xiong Y, Cao YL, Ai XP, Yang HX. Synergistic Na-storage reactions in Sn_4P_3 as a high-capacity, cycle-stable anode of Na-ion batteries. Nano Lett. 2014;14(4):1865.
[19] Liu SL, Zhang HZ, Xu LQ, Ma LB. Synthesis of hollow spherical tin phosphides (Sn_4P_3) and their high adsorptive and electrochemical performance. J Crystal Growth. 2016;438:31.
[20] Zhang JL, Wang WH, Li BH. Effect of particle size on the sodium storage performance of Sn_4P_3. J Alloys and Compounds. 2019;771:204.
[21] Meng RJ, Deng QY, Peng CX, Chen BJ, Liao KX, Li LJ, Yang ZY, Yang DL, Zheng L, Zhang C, Yang JH. Two-dimensional organic-inorganic heterostructures of in situ-grown layered COF on Ti_3C_2 MXene nanosheets for lithium-sulfur batteries. Nano Today. 2020;35:100991.
[22] Meng RJ, Huang JM, Feng YT, Zu LH, Peng CX, Zheng LR, Zheng L, Chen ZB, Liu GL, Chen BJ, Mi YL, Yang JH. Black phosphorus quantum dot/Ti_3C_2 MXene nanosheet composites for efficient electrochemical lithium/sodium-ion storage. Adv Energy Mater. 2018;8(26):1801514.
[23] Ming FW, Liang HF, Huang G, Bayhan Z, Alshareef HN. MXenes for rechargeable batteries beyond the lithium-ion. Adv Mater. 2021;33(1):2004039.
[24] Kajiyama S, Szabova L, Sodeyama K, Iinuma H, Morita R, Gotoh K, Tateyama Y, Okubo M, Yamada A. Sodium-ion intercalation mechanism in MXene nanosheets. ACS Nano. 2016;10(3):3334.
[25] Li K, Liang MY, Wang H, Wang XH, Huang YS, Coelho J, Pinilla S, Zhang YL, Qi FW, Nicolosi V, Xu YX. 3D MXene architectures for efficient energy storage and conversion. Adv Funct Mater. 2020;30(47):2000842.
[26] Zhao DY, Zhao RZ, Dong SH, Miao XG, Zhang ZW, Wang CX, Yin LW. Alkali-induced 3D crinkled porous Ti_3C_2 MXene architectures coupled with NiCoP bimetallic phosphide nanoparticles as anodes for high-performance sodium-ion batteries. Energy Environ Sci. 2019;12(8):2422.
[27] Hui XB, Zhao RZ, Zhang P, Li CX, Wang CX, Yin LW. Low-temperature reduction strategy synthesized Si/Ti_3C_2 MXene composite anodes for high-performance Li-ion batteries. Adv Energy Mater. 2019;9(33):1901065.
[28] Li JH, Rui BL, Wei WX, Nie P, Chang LM, Le ZY, Liu MQ, Wang HR, Wang LM, Zhang XG. Nanosheets assembled layered MoS_2/MXene as high performance anode materials for potassium ion batteries. J Power Sources. 2020;449:227481.
[29] Zhao TK, Zhang JK, Du Z, Liu YH, Zhou GL, Wang JT. Dopamine-derived N-doped carbon decorated titanium carbide composite for enhanced supercapacitive performance. Electrochim Acta. 2017;254:308.
[30] Pan ZH, Cao F, Hu X, Ji XH. A facile method for synthesizing CuS decorated Ti_3C_2 MXene with enhanced performance for asymmetric supercapacitors. J Mater Chem A. 2019;7(15):8984.
[31] Guo X, Zhang WX, Zhang JQ, Zhou D, Tang X, Xu XF, Li BH, Liu H, Wang GX. Boosting sodium storage in two-dimensional phosphorene/$Ti_3C_2T_x$ MXene nanoarchitectures with stable fluorinated interphase. ACS Nano. 2020;14(3):3651.
[32] Pan E, Jin YH, Zhao CC, Jia M, Chang QQ, Jia MQ. Dopamine-derived N-doped carbon encapsulating hollow Sn_4P_3 microspheres as anode materials with superior sodium storage performance. J Alloys Compd. 2018;769:45.
[33] Liu YT, Zhang P, Sun N, Anasori B, Zhu QZ, Liu H, Gogotsi Y, Xu B. Self-assembly of transition metal oxide nanostructures on MXene nanosheets for fast and stable lithium storage. Adv Mater. 2018;30(23):e1707334.
[34] Li H, Chen R, Ali M, Lee H, Ko MJ. In situ grown MWCNTs/MXenes nanocomposites on carbon cloth for high-performance flexible supercapacitors. Adv Funct Mater. 2020;30(47): 2002739.
[35] Ran LB, Luo B, Gentle IR, Lin TE, Sun Q, Li M, Rana MM, Wang LZ, Knibbe R. Biomimetic Sn_4P_3 anchored on carbon nanotubes as an anode for high-performance sodium-ion batteries. ACS Nano. 2020;14(7):8826.
[36] Liu Q, Ye JJ, Chen ZZ, Hao Q, Xu CX, Hou JG. Double conductivity-improved porous Sn/Sn_4P_3@carbon nanocomposite as high performance anode in lithium-ion batteries. J Colloid Interface Sci. 2019;537:588.
[37] Fan L, Ma RF, Wang J, Yang HG, Lu BA. An ultrafast and highly stable potassium-organic battery. Adv Mater. 2018; 30(51):e1805486.
[38] Huang KS, Xing Z, Wang LC, Wu X, Zhao W, Qi XJ, Wang H, Ju ZC. Direct synthesis of 3D hierarchically porous carbon/Sn composites via in situ generated NaCl crystals as templates for potassium-ion batteries anode. J Mater Chem A. 2018;6(2):434.
[39] Wang H, Xing Z, Hu ZK, Zhang Y, Hu Y, Sun YW, Ju ZC, Zhuang QC. Sn-based submicron-particles encapsulated in porous reduced graphene oxide network: advanced anodes for high-rate and long life potassium-ion batteries. Appl Mater Today. 2019;15:58.
[40] Zhao XX, Wang WH, Hou Z, Wei GJ, Yu YK, Zhang J, Quan Z. $SnP_{0.94}$ nanoplates/graphene oxide composite for novel potassium-ion battery anode. Chem Eng J. 2019;370:677.